Earthquake Spectra

RESEARCH PAPER

Impact of Seismic Wave Types on the Response of Near-Fault Valley-Spanning Bridges

Chao Luo[1,2] | Jingjing Li[2] | Zhipeng Zhao[3] | Hao Wang[1,2]

[1]Key Laboratory of Roads and Railway Engineering Safety Control, Ministry of Education, Shijiazhuang Tiedao University, Shijiazhuang, China | [2]School of Civil Engineering, Shijiazhuang Tiedao University, Shijiazhuang, China | [3]Department of Disaster Mitigation for Structures, Tongji University, Shanghai, China

Correspondence: Hao Wang (wanghao@stdu.edu.cn)

Received: 29 January 2025 | **Revised:** 3 September 2025 | **Accepted:** 8 October 2025

Keywords: arch bridge | ground motion | nonuniform excitation | physics-based source model | seismic response | V-shaped valley

ABSTRACT

The complex terrain and expanding transport networks in Southwest China have heightened the demand for valley-spanning bridges in active fault zones, posing seismic design challenges. This study investigates the seismic response of a near-fault valley-spanning bridge using deterministic ground motion simulations of reverse fault rupture. The goal is to evaluate whether the common seismic design assumption that horizontal and vertical ground motions can be represented by SV and P waves is consistent with actual conditions represented by the fully 3D waveform solution and to assess the validity of assuming Rayleigh waves as input waves. Results indicate significant differences in the internal forces. Axial force distribution varied: The fully 3D waveform solution and Rayleigh wave caused peak axial forces near the arch crown and arch foot, while the P–SV wave caused peaks mainly near the arch foot. Analysis of transfer functions for axial forces at the arch foot revealed that these differences are attributed to variations in the dominant mode shapes excited by different inputs: The fully 3D waveform solution predominantly excited longitudinal and transverse rotational modes, Rayleigh wave primarily excited transverse rotational modes, and P–SV wave mainly excited longitudinal and vertical modes. These findings underscore that treating seismic motions as single Rayleigh or P–SV waves may cause overestimation or underestimation of the structural response. Therefore, the fully 3D waveform solution is recommended for reliable near-fault seismic response assessment and design of valley-spanning bridges in complex terrain.

1 | Introduction

The topography of river valleys significantly impacts the distribution of seismic hazards due to its topographic effects (Verret et al. 2021; Podestá et al. 2019). These effects expose bridge piers or bearings at different locations to significant nonuniform seismic excitation. The wave propagation patterns, attenuation effect, incoherence effect, and site-response effect can cause spatial variations in ground motion (Sextos et al. 2003). Nonuniform seismic excitation significantly affects the seismic response of long-span bridge structures (Xiong et al. 2018; Chouw and Hao 2008; Efthymiou and Camara 2022). Irregular river valley topography can cause seismic wave scattering. Scattered waves superpose with incident and reflected waves, leading to the amplification or attenuation of ground motion at different locations (Gao et al. 2021), thereby increasing the nonuniformity of ground motion.

Numerous researchers have investigated the seismic response of bridges crossing river valleys. Li et al. (2023) constructed two-dimensional V-shaped valley-bridge models with varying depths and half-width ratios, revealing that the amplification and attenuation effects of valleys on incident seismic waves significantly depend on these geometric parameters. Zhang et al. (2024) investigated the seismic responses of bridges spanning V-shaped valleys subjected to shear horizontal (SH) waves and found that valley topography amplifies seismic responses of both the bridge and its wave-facing side, increasing the peak ground acceleration (PGA) of the bridge by more than 35%. Liu et al. (2021) investigated the effect of spatially varying multisupport excitation under shear vertical (SV) wave incidence on the seismic response of bridge structures, finding that the spatial variability of ground motions under oblique SV wave multisupport excitation significantly increases the amplitude of the computed results. Zhou et al. (2010) analyzed the seismic responses of a rigid-frame bridge crossing a river valley, demonstrating that under oblique SV wave incidence, vibrations on valley slopes perpendicular to the direction of wave propagation are notably stronger than those on the opposite slope, accompanied by greater surface deformation. Most existing studies have focused on the impact of valley terrain effects on the seismic response of valley-spanning bridges under SV wave incidence. However, different types of seismic waves exhibit distinct characteristics in the distribution of ground motion across valley sites (Luzón et al. 1997; Wong 1982; Ding et al. 2017). Li et al. (2022) examined the spatial variation of PGA in V-shaped valleys under the influence of SV waves, concluding that the seismic motion characteristics are uniform on both sides of a valley, with the vertical seismic motion peak at a valley bottom close to 0. When Rayleigh waves are incident, Ba and Liang (2015) studied the effect of oblique Rayleigh wave incidence on concave terrain seismic effects. It was found that the steepness of the terrain on the wave-facing side is directly proportional to the peak ground displacement, and the shielding effect of the terrain on Rayleigh waves increases with depth. The above research indicates that SV wave incidence leads to uniform ground motion across the valley, whereas Rayleigh waves induce significant nonuniformity between the two sides. The differences in site effects caused by SV and Rayleigh waves can result in varying ground motion inputs for large-span bridges, leading to different seismic responses in these structures.

Natural seismic motion consists of various types of seismic waves, including body waves (such as primary waves and secondary waves) and surface waves (such as Rayleigh and Love waves). Among these, Rayleigh waves have low frequencies and slow attenuation rates. At sites farther from the epicenter, Rayleigh waves dominate in energy (Liu and Li 2006). Currently, research on the impact of Rayleigh waves on the seismic response of bridge structures is still limited. Gu and Yu (2011) investigated the dynamic interaction between pile–soil–bridge structures under Rayleigh wave action, revealing that high-frequency Rayleigh waves produce much larger horizontal and vertical displacements than low-frequency Rayleigh waves. Betti et al. (1993) examined the seismic response of bridge structures considering soil–structure interaction, including SH waves, P waves, SV waves, and Rayleigh waves. The results indicated that Rayleigh waves have a significantly greater influence on the seismic response of bridge structures than the other three wave types. Somaini (1987) studied the seismic performance of beam bridges under horizontal traveling wave excitation, showing that Rayleigh waves induce both translational and rotational excitation in the bridge structure, increasing deformation and relative motion between structural elements. These studies all indicate that Rayleigh waves can lead to increased internal forces and deformations in structures compared to body waves such as P, SV, or SH waves. This study builds upon the findings in the literature (Luo, Sheng et al. 2024) to further analyze the impact of fully 3D waveform solution on the seismic response of valley-spanning bridges. It compares these effects with those of Rayleigh and SV wave incidences, aiming to deepen the understanding of the mechanisms by which seismic waves affect the seismic response of valley-spanning bridges and enhance the theoretical framework for seismic design calculations.

In summary, most existing studies have focused on the influence of valley topography on the seismic response of valley-spanning bridges under SV wave incidence, while the effects of Rayleigh wave incidence under such conditions have received relatively little attention. These studies are mostly based on the assumption that horizontal and vertical ground motions are represented by SV and P waves, respectively, in seismic design. However, the extent to which this assumption holds when accounting for source rupture, wave propagation, and site effects requires further investigation. Since seismic motion on both sides of the valley is uniform under SV wave incidence, these studies do not address the nonuniform excitation issue in valley-spanning bridges. In actual strong earthquake observations, a phenomenon known as the backslope amplification effect is observed. This refers to the more significant amplification of ground motion on the backslope side compared to the front slope side in valleys with slopes nearly perpendicular to the fault rupture zone (He et al. 2015; Wang et al. 2018). Under the incidence of the Rayleigh wave, the backslope amplification effect introduces significant spatial variations in seismic motion between the two sides of the valley, which aligns more closely with observed strong seismic motion records. Natural seismic motion is not composed of a single type of wave. Currently, many studies use simulated or artificially synthesized seismic motions to analyze the seismic response of structures. Zhang et al. (2020) and Jia et al. (2024) examined the effect of synthetic seismic motions on the seismic response of cross-fault bridges. Additionally, numerous researchers have applied physics-based numerical methods to simulate seismic motions

(Rosti et al. 2023; Latečki et al. 2021; Girmay et al. 2024; Kenawy et al. 2023; Wang et al. 2024; Gatti et al. 2018; McCallen, Petersson et al. 2021; McCallen, Petrone et al. 2021; Zhang et al. 2023; Luo, Cao et al. 2024; Luo et al. 2026) in structural seismic response analysis. However, the impact of fully 3D waveform solution on the seismic response of valley-spanning bridges requires further investigation. This study uses the SW4 (seismic waves, fourth order) finite difference software (Sjögreen and Petersson 2012; Petersson and Sjögreen 2017a, 2017b) and the GP (Graves and Pitarka) kinematic rupture model (Graves and Pitarka 2004, 2010, 2015, 2016; Pitarka et al. 2020, 2022) to simulate fully 3D waveform solution. The study focuses on a large-span, steel–concrete arch bridge spanning a V-shaped valley. It compares the seismic response of the valley-spanning bridge under the fully 3D waveform solution, Rayleigh wave, and SV wave inputs, to evaluate the validity of assuming horizontal and vertical ground motions as body waves (SV and P waves) and Rayleigh waves, respectively. At the same time, it explores the response patterns of the upper concrete-filled steel tube arch bridge under different seismic wave types.

2 | Project Overview and Computational Model

This study focuses on a large-span, upper-deck steel pipe concrete arch bridge spanning a V-shaped valley, as shown in Figure 1. The bridge has a rise of 90 m and a main span of 504 m. Both the upper and lower chord members of the main arch ribs, as well as the arch axis, are designed using a catenary curve with an arch axis coefficient of 1.55. The main arch ring is designed as an equal-width, variable-height space truss structure. The upper and lower chord members of the main arch ribs are made of steel pipe concrete, with Q420ND steel pipes filled with C60 self-compacting expansive concrete. The deck system of the main bridge consists of a continuous composite slab structure with spans of 33.6 m × 15 m.

A finite element model of the valley–arch bridge interaction is established based on engineering data. The bridge deck, vertical arch columns, and main arch ring are simulated using Timoshenko beam elements. The three-dimensional site model is represented using eight-node brick elements. According to research by Kuhlemeyer and Lysmer (1973), for wave propagation simulations using finite element methods, the element mesh should not exceed 1/8 of the minimum wavelength of the simulated seismic motion. In this study, the minimum shear wave velocity of the site is 2000 m/s, the highest simulated seismic motion frequency is 10 Hz, and the minimum seismic motion wavelength to be simulated is 200 m. To minimize mesh size effects and accurately model the terrain and bridge–valley coupling, the mesh size of the calculation model is set to 15 m. According to Luo et al. (2019), when the ratio of the local site model width to the valley width exceeds 2, the modified domain reduction method (MDRM) (Luo et al. 2019), combined with viscoelastic artificial boundaries, limits the relative PGA error to below 5%. In this study, the valley depth is 225 m, the horizontal distance between the riverbanks is 450 m, and the main span of the bridge is 504 m. The minimum width of the computational model is calculated as 1008 m and is set to 1020 m. A schematic of the computational range for the valley–arch bridge interaction system is shown in Figure 2a. The lateral direction (*x*-direction in Figure 2b) of the model is not affected by topographical effects, and the lateral width of the valley model is set to be no less than the valley depth Luo, Sheng et al. (2024). In this study, the valley width is set to 510 m. The positions of the arch feet are simulated by defining constraint equations to

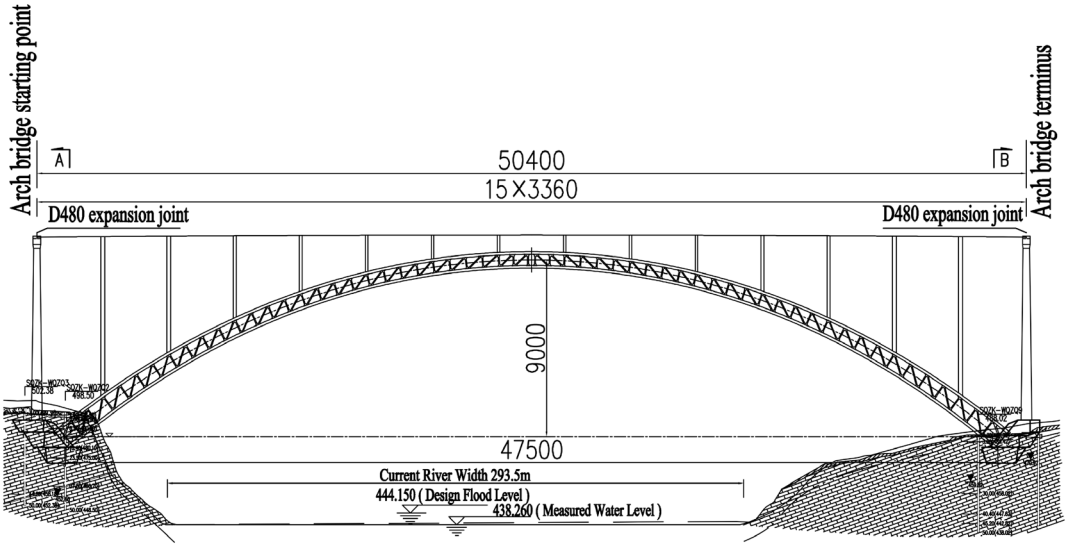

FIGURE 1 | Elevation layout of river valley arch bridge.

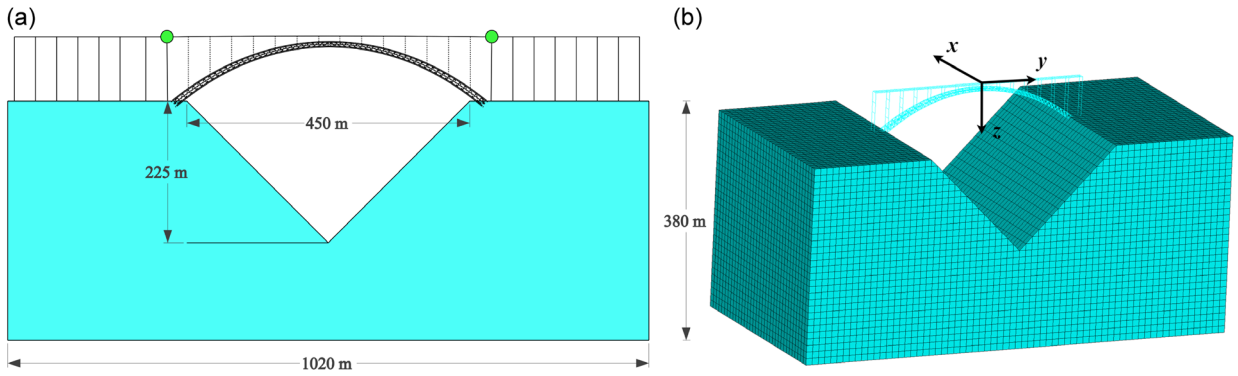

FIGURE 2 | Valley–arch bridge model: (a) schematic diagram of the calculation range of the river valley–arch bridge interaction system and (b) bridge–valley interaction finite element model.

create rigid zones between the beam elements and valley solid elements, anchoring the arch feet to the mountain and connecting the arch bridge to the valley terrain. Since the main bridge and approach bridge are separated by the junction pier, the junction pier is located at the point in Figure 2a. This study models only the main bridge and includes a concentrated mass at the junction pier to account for the approach bridges. The finite element model of the valley–arch bridge interaction system is shown in Figure 2b.

3 | Seismic Motion Input

To study the influence of the fully 3D waveform solution, Rayleigh wave, and SV wave on the seismic response, this study assumes that all three types of waves have the same free-field ground motion at the wave-facing side. This assumption facilitates comparing the seismic response to the fully 3D waveform solution, Rayleigh wave, and SV wave. Considering the phase differences in the free-field ground motion of the fully 3D waveform solution and Rayleigh wave at the surface during propagation, the model is designed to have the same ground motion at the wave-facing side, as described in the section Characteristics of Ground Motion Field Distribution. For the SV wave input case, the horizontal component of the seismic motion is introduced as a vertically incident SV wave, while the vertical component is introduced as a vertically incident P wave. Both components have amplitudes consistent with the fully 3D waveform solution. This case, where the horizontal component is input as SV wave and the vertical component as P wave, is referred to as the P–SV wave input case.

3.1 | Seismic Motion Simulation

This study discusses the effect of earthquakes on the seismic response of a valley-spanning bridge subjected to an earthquake on a reverse fault-oriented perpendicular to the longitudinal direction of the bridge. First, a deterministic seismic motion simulation is performed to obtain the fully 3D waveform solution. The SW4 finite difference software is used for seismic motion simulation (Sjögreen and Petersson 2012; Petersson and Sjögreen 2017a, 2017b), with the GP kinematic rupture model selected for the fault rupture model (Graves and Pitarka 2004, 2010, 2015, 2016; Pitarka et al. 2020, 2022). The simulated earthquake has a magnitude of 6, with a source depth of 8.12 km, a dip angle of 60°, and a rake angle of 90°, and the subfault size is 0.1 km (Rodgers et al. 2020). The fault measures 14.2 km in length and 7.2 km in width, and the top of the rupture surface (the shallowest boundary of the fault plane) is located at a depth of 5 km. The fault strikes to the north and is a reverse fault. The distribution of slip on the fault plane generated using the GP kinematic rupture model is shown in Figure 3a. The relative positions of the fault, valley, and bridge are illustrated in Figure 3b. The soil layers are horizontally layered, and the 1D velocity model is provided in Table 1.

3.2 | Seismic Motion Input Method

The MDRM (Luo et al. 2019) shown in Figure 4 is used to apply loading to the valley–arch bridge interaction model. In Figure 4, the blue area, denoted as Ω, represents the region of interest for computation. The black area, labeled as Ω^+, indicates the remaining semi-infinite exterior subdomain, while the red area, referred to as Γ, represents the interface

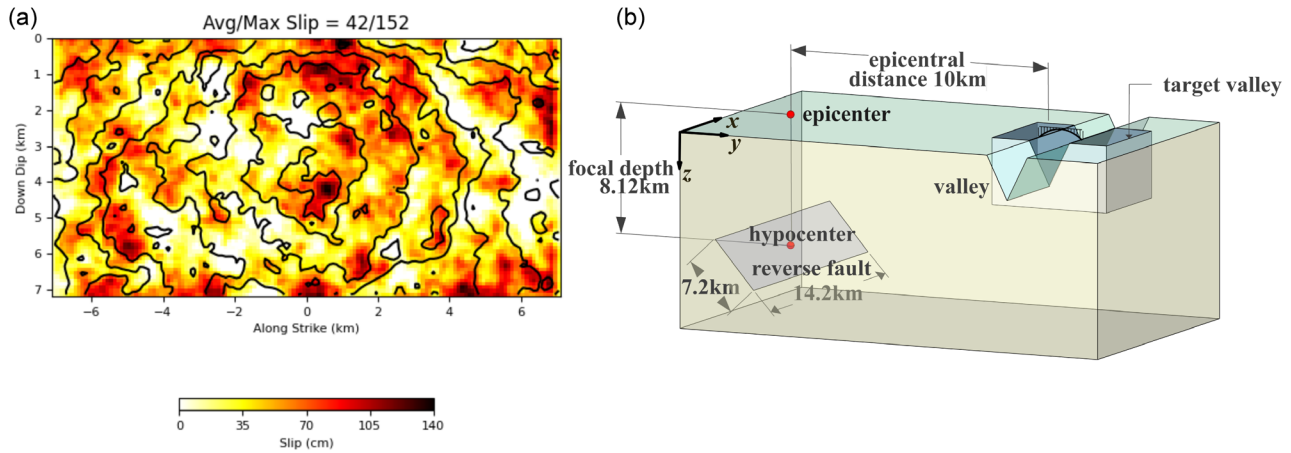

FIGURE 3 | Fault rupture model and spatial relationship: (a) fault rupture slip distribution diagram and (b) relative location diagram of fault, valley, and bridge.

TABLE 1 | 1D velocity model information.

Soil layer depth, km	Shear wave velocity, km/s	Compressional wave velocity, km/s	Density, kg/m^3	Quality factor Qs	Quality factor Qp
0.00	2.00	3.50	2450	200	100
1.50	2.10	4.20	2575	210	105
2.50	2.40	4.75	2600	240	120
3.50	2.75	5.10	2620	276	138
5.00	3.00	5.40	2650	300	150
7.00	3.35	5.80	2700	336	168
9.00	3.50	6.20	2720	350	175
17.00	3.60	6.35	2750	360	180
30.00	3.80	6.80	3000	380	190

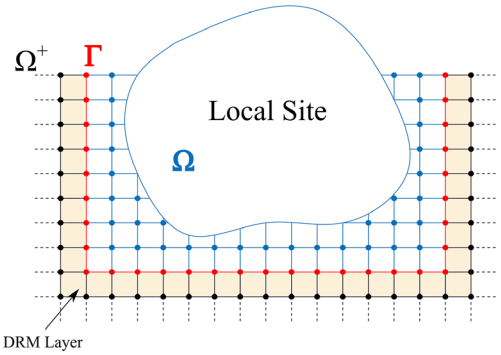

FIGURE 4 | Schematic diagram of the modified domain reduction method.

between the region of interest and the other regions in the system. Typically, the local site lies within region Ω^+, far from the fault. The equivalent force load of the MDRM can be expressed as

$$P_{\text{eff}}^{\text{MDRM}} = \begin{Bmatrix} 0 \\ -M_{be}^{\Omega+}\ddot{u}_e^0 - C_{be}^{\Omega+}\dot{u}_e^0 - K_{be}^{\Omega+}u_e^0 \\ M_{eb}^{\Omega+}\ddot{u}_b^0 + C_{eb}^{\Omega+}\dot{u}_b^0 + K_{eb}^{\Omega+}u_b^0 \end{Bmatrix} \quad (1)$$

In Equation (1), the first, second, and third rows of the vector represent the equivalent loads in the regions of nodes i, b, and e, respectively. M, C, and K represent the mass matrix, damping matrix, and stiffness matrix of the system, respectively; the subscripts i, b, and e represent the nodes on the regions Ω, Γ, and Ω^+, while u^0 represents the free-field displacement response. For a detailed derivation of Equation (1), readers are referred to Luo et al. (2019).

The MDRM effectively simulates the area within Ω, but residual displacement fields remain in the Ω^+ region. To prevent interference from these residual displacement fields, artificial boundaries are placed at the outer model boundaries to absorb them. When applying the improved regional reduction method, the free-field time history at the boundary nodes is first calculated, followed by the calculation of the equivalent force load using Equation (1), which then loads the finite element model.

3.3 | Calculation Methods for Rayleigh Waves

The seismic motion time history at the boundary points under Rayleigh wave incidence can be calculated using the approximate methods proposed by Yue and Li (2008) and Zhao et al. (2022). The approximate method uses potential functions to solve the Rayleigh wave fluctuation equation. The acceleration at the position with identical ground motion at the outer wave-facing side is taken as the known acceleration. By integrating this acceleration, the displacement time history is obtained, which is then used to calculate the seismic motion time history at any point using the analytical solution for Rayleigh waves.

The process begins by using the Rayleigh wave fluctuation equation to solve the Rayleigh wave velocity c. The Rayleigh wave fluctuation equation is expressed as follows:

$$(2-c^2/{V_S}^2)^2-4\sqrt{1-c^2/{V_S}^2}\cdot\sqrt{1-c^2/{V_P}^2}=0 \tag{2}$$

where V_P, V_S, and c represent the compressional wave velocity, shear wave velocity, and Rayleigh wave velocity, respectively.

Using Equation (2), based on the fluctuation equation and potential functions, and considering the real part of the displacement, the expression for a simple harmonic Rayleigh wave can be obtained:

$$\begin{aligned} u_y &= -Ak\left[\exp(-akz)-\frac{(1+b^2)}{2}\exp(-bkz)\right]\sin(k(y-ct)) \\ u_z &= Ak\left[-a\exp(-akz)+\frac{(1+b^2)}{2b}\exp(-bkz)\right]\cos(k(y-ct)) \end{aligned} \tag{3}$$

where u_y and u_z represent the horizontal and vertical displacements, respectively, A is the amplitude parameter, k is the wave number, ω is the angular frequency, $a=\sqrt{1-c^2/{V_P}^2}$, and $b=\sqrt{1-c^2/{V_S}^2}$.

Then, by applying the Fourier transform, the displacement time history at the boundary points is expressed as a superposition of simple harmonic waves, allowing the calculation of the seismic motion time histories at any position in the model in the frequency domain. Finally, the inverse Fourier transform is applied to obtain the seismic motion time histories at any position in the time domain.

4 | Analysis Cases

To study the seismic impact of fully 3D waveform solution, Rayleigh wave, and P–SV wave on bridge structures and compare their seismic responses, three calculation cases are designed, as shown in Table 2.

TABLE 2 | Calculation cases.

Case	Types of seismic wave	Computational model
1	Fully 3D waveform solution	Valley–arch bridge model
2	Rayleigh wave	Valley–arch bridge model
3	P–SV wave	Valley–arch bridge model

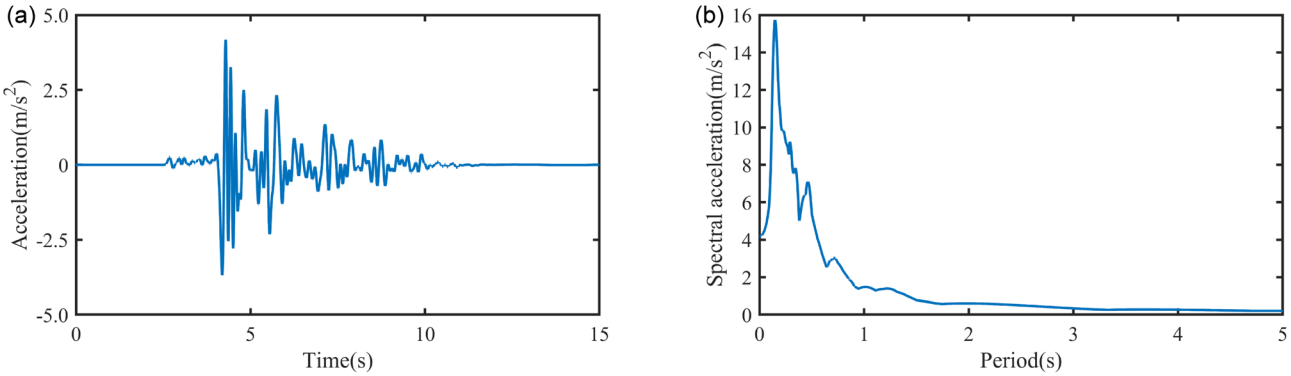

FIGURE 5 | Horizontal acceleration characteristics at the reference location with identical ground motion: (a) acceleration histories and (b) acceleration response spectra.

Seismic waves are input from the outer side of the model in the form of the fully 3D waveform solution, Rayleigh wave, and P–SV wave. It is assumed that all three types of waves have the same ground motion at the reference location outer side of the model, ensuring that the results for these wave types are comparable. The free-field horizontal acceleration time histories and acceleration response spectra are shown in Figure 5. The acceleration time histories and response spectra at ground surface locations on both sides of the valley under Cases 1, 2, and 3 are presented in Figure 6. As described in the previous section, the free-field time histories at the boundary nodes are converted into equivalent force loads via the MDRM and applied to the finite element model, thereby introducing the fully 3D waveform solution. The calculation area of the valley–arch bridge interaction model is shown in Figure 3b. For the fully 3D waveform solution input case, seismic motion is simulated to obtain the acceleration, velocity, and displacement time histories. The equivalent loads are then calculated using Equation (1) based on the mass, stiffness, and damping matrices of the finite element model, thus achieving the fully 3D waveform solution input. For the Rayleigh wave input case, after calculating the seismic motion time history at the boundary nodes using the approximate Rayleigh wave method described in section Calculation Methods for Rayleigh Waves, the MDRM is applied to account for the valley terrain effects. The equivalent loads are then computed using Equation (1), thereby introducing the Rayleigh wave ground motions into the finite element model.

For the P–SV wave input case, the horizontal and vertical components have amplitudes consistent with the fully 3D waveform solution. For this case, the incident wave time history at the bottom of the model is calculated using one-dimensional wave inversion (Wang and Chen 2016). Subsequently, the free-field time history at any depth is obtained through one-dimensional wave propagation analysis. This data is substituted into Equation (1) to calculate the equivalent loads, thereby introducing the P–SV wave ground motions into the finite element model.

5 | Computational Results

5.1 | Reliability Verification of the GP Kinematic Rupture Model

To verify the accuracy of the GP kinematic rupture model and the wave propagation simulation used in this study, we compared the east–west (*y*-direction) and north–south (*x*-direction) PGA at observation points located within a region defined by the fault length in the strike direction and 50 km in the direction perpendicular to the fault. The simulated PGA values were compared with those predicted by the ground motion prediction equation (GMPE) developed by Chiou and Youngs (2008) (hereafter referred to as CY2008).

Figure 7 illustrates the attenuation of horizontal PGA from the fully 3D waveform solution with increasing epicentral distance. The solid line represents the median prediction from the GMPE, while the dashed lines indicate ± 1 standard deviation. As shown in Figure 7, the horizontal PGA values from the fully 3D waveform solution generally fall within one standard deviation of the predicted median, indicating that the selected rupture model is physically reasonable and that the wave propagation simulation is highly accurate. Therefore, the fully 3D waveform solution used in this study is deemed appropriate and capable of representing near-fault ground motions under the considered scenario.

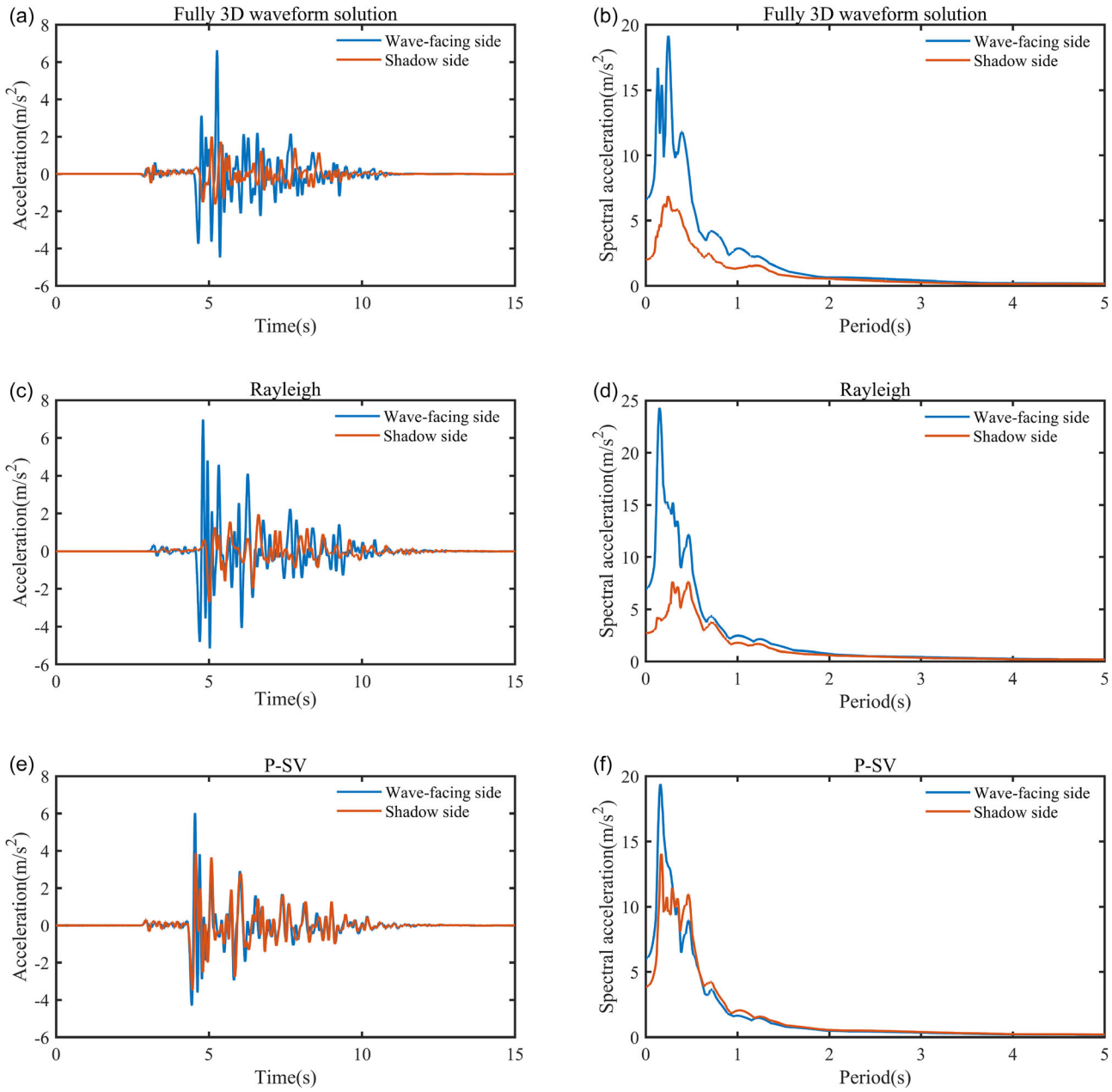

FIGURE 6 | Acceleration time histories and response spectra on both sides of the valley (Cases 1–3): (a,c,e) acceleration time histories and (b,d,f) acceleration response spectra at wave-facing and shadow sides of the valley for Cases 1, 2, and 3, respectively.

5.2 | Characteristics of Ground Motion Field Distribution

Figure 8 shows the distribution of the horizontal direction PGA of the fully 3D waveform solution. As seen in Figure 8a, within the range from the fault to the valley, the PGA in the *x*-direction exhibits larger amplitudes for *x* greater than 10 km, with significant values at the valley location. From Figure 8b, it can be seen that in the *y*-direction, between the fault and the valley, the PGA in the *y*-direction of the fully 3D waveform solution is higher in the central area and lower in the peripheral regions. Overall, at the *y*-coordinate of 12.7 km (corresponding to the valley location), a sharp spatial variation in the seismic motion is observed, with the ground motion being smaller in the valley terrain and larger on both sides of the valley.

To examine the effect of the valley terrain on the seismic response of the structure, this study selects the bridge site location at the position where the ratio of PGA on the wave-facing side to the shadow side is maximized. Specifically, the river valley extends from 10.200 km in the *x*-direction and from 12.705 to 13.155 km in the *y*-direction, as indicated by the straight line within the dashed box in Figure 8. To compare the effects of different types of seismic waves on the valley terrain, the PGA at the surface near the valley was first calculated for three types of seismic wave

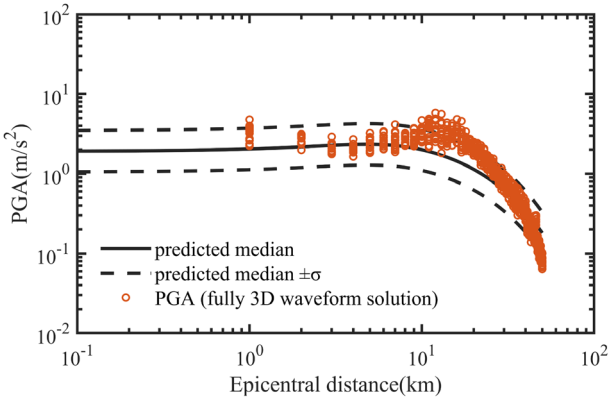

FIGURE 7 | Distribution of horizontal PGA attenuation at observation points from the fully 3D waveform solution versus epicentral distance.

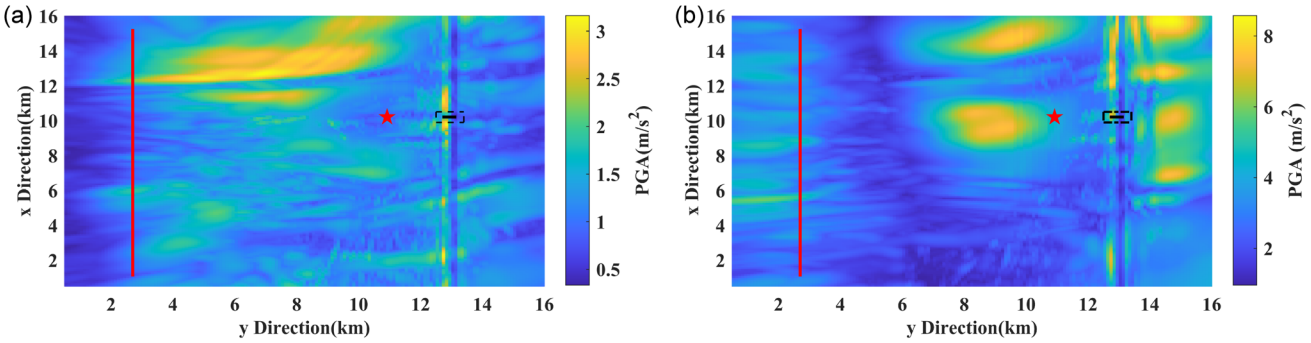

FIGURE 8 | PGA distribution map for the fully 3D waveform solution. The red straight line represents the projection of the geometric center of the fault rupture surface along the fault strike onto the ground surface upper fault trace. The red star denotes the reference location where the input acceleration time histories of the full 3D waveform solution, Rayleigh wave, and P–SV wave exactly match. This reference point is located 2 km from the center of the valley: (a) *x*-direction (north–south) and (b) *y*-direction(east–west).

inputs. Figure 9 shows the spatial variation of PGA values across the V-shaped valley site under the 3D simulated, Rayleigh, and P–SV wave cases. The lowest point of the valley is designated as the origin of the horizontal coordinate, and the dashed line represents the position of the V-shaped valley. Table 3 lists the PGA at the surface locations on the tops of the slopes on both sides under the loading imposed by the fully 3D waveform solution, Rayleigh wave, and P–SV wave.

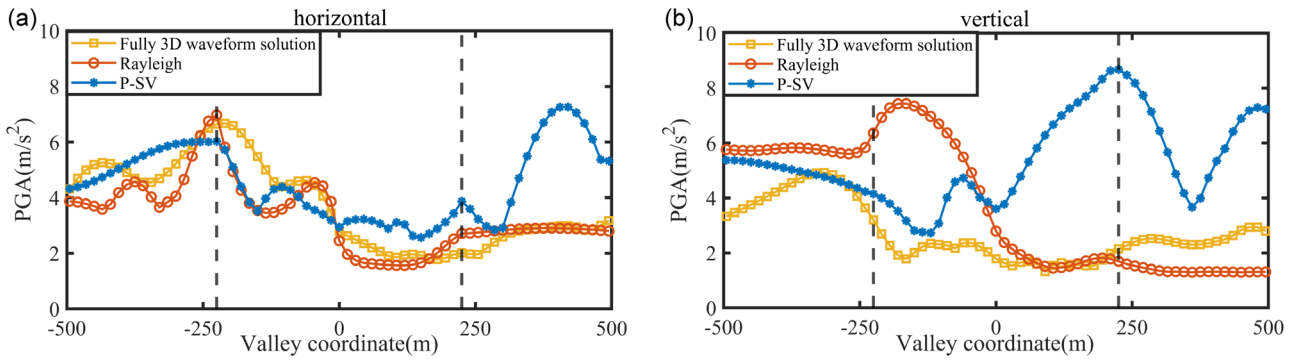

FIGURE 9 | Peak value distribution of ground motion of fully 3D waveform solution, Rayleigh wave, and P–SV waves: (a) horizontal direction and (b) vertical direction.

TABLE 3 | Peak value of ground motion acceleration of bridge piers on both sides of fully 3D waveform solution, Rayleigh wave, and P–SV wave.

	Observation location	Fully 3D waveform solution	Rayleigh wave	P–SV wave
Horizontal seismic motion	Wave-facing side	6.64	6.97	6.02
	Shadow side	2.01	2.71	3.87
	Wave-facing side/shadow side	3.30	2.57	1.56
Vertical seismic motion	Wave-facing side	3.20	6.36	4.15
	Shadow side	2.15	1.69	8.68
	Wave-facing side/shadow side	1.49	3.76	0.48

From Table 3 and Figure 9a, it can be observed that under the loading imposed by the 3D simulated waveforms, there is a significant spatial variation in horizontal PGA values on both sides of the V-shaped valley. The horizontal PGA on the wave-facing side is much higher than on the shadow side. The maximum horizontal PGA occurs near the top of the wave-facing side slope, and the horizontal PGA on the wave-facing side is 3.30 times greater than that on the shadow side. Under the incidence of the Rayleigh wave, the distribution of horizontal PGA is similar to that of the fully 3D waveform solution, with the maximum PGA at the top of the wave-facing side slope. Here, the horizontal PGA on the wave-facing side is 2.57 times that on the shadow side. Under the incidence of the P–SV wave, the PGA values at surface locations on both sides of the V-shaped valley is nearly symmetrical. The maximum horizontal PGA occurs near the flat surface at the top of the shadow side slope, with relatively lower values at the valley bottom. In this case, the horizontal PGA on the wave-facing side is 1.56 times that on the shadow side.

From Table 3 and Figure 9b, it can be observed that under the incidence of the fully 3D waveform solution, the vertical PGA on both sides of the V-shaped valley exhibits little variation. The maximum vertical PGA occurs near the flat area at the top of the wave-facing side slope, while the minimum is near the valley bottom. The vertical PGA on the wave-facing side is 1.49 times that on the shadow side. Under the incidence of the Rayleigh wave, a significant difference is observed in the vertical PGA distribution, with the vertical PGA on the wave-facing side much higher than on the shadow side. The maximum vertical PGA occurs at the top of the wave-facing side slope, where the vertical PGA on the wave-facing side is 3.76 times that on the shadow side. Under the incidence of the P–SV wave, the vertical PGA on the wave-facing side is much smaller than on the shadow side, with the maximum vertical PGA at the top of the shadow side slope. In this case, the vertical PGA on the wave-facing side is only 0.48 times that on the shadow side.

It can be observed that the valley terrain weakens the incident waves on the shadow side, and this shielding effect is more significant when subjected to the fully 3D waveform solution and Rayleigh wave incidence. This results in significant differences in the surface PGA on both sides of the slope during the incidence of fully 3D waveform solution and Rayleigh wave, with the PGA on the wave-facing side being significantly greater than that on the shadow side. The shielding effect of valley terrain significantly affects the seismic response of valley-spanning bridge structures.

5.3 | Impact of Fully 3D Waveform Solution on Bridge Seismic Response

This section discusses the influence of the fully 3D waveform solution on the seismic response of the arch bridge. To compare the three cases, dimensionless parameters γ_{SR} and γ_{SS} are introduced, where γ_{SR} represents the ratio of the internal forces of the bridge under the loading imposed by the 3D simulated waveforms to that under the Rayleigh wave and γ_{SS} represents the ratio of the internal forces of the bridge under the loading imposed by the 3D simulated waveforms to that under the P–SV wave:

$$\gamma_{SR} = N_{SW4}/N_R \tag{4}$$

$$\gamma_{SS} = N_{SW4}/N_S \tag{5}$$

where N_{SW4}, N_R, and N_S represent the structural response of the member under the fully 3D waveform solution, Rayleigh wave, and P–SV wave incidences, respectively.

5.3.1 | Impact of Fully 3D Waveform Solution on Arch Ring Internal Forces

Table 4 lists the peak internal forces of the arch ring subjected to the loading imposed by the 3D simulated waveforms, Rayleigh wave, and P–SV wave, all corresponding to an epicentral distance of 10 km. Figure 10 illustrates the distribution of these responses in the upper and lower chord members of the main arch ring under the three types of wave incidences. From Figure 10a and Table 4, it is observed that compared with Rayleigh wave incidence, the axial forces of the upper and lower chord members are smaller when subjected to the loading imposed by the 3D simulated waveforms. Specifically, the peak axial forces of the upper and lower chord members are 0.71 times and 0.75 times, respectively, compared to those under Rayleigh wave incidence. Under Rayleigh wave input, the peak axial force of the upper chord is approximately 41% higher than that under the fully 3D waveform solution. Compared to P–SV wave incidence, the axial force of the upper chord member is amplified by 1.26 times under the fully 3D waveform solution, while the peak axial forces of the lower chord members in both cases are relatively close. The amplification of the peak axial force of the upper chord member due to the fully 3D waveform solution is greater than that of the lower chord member. Under P–SV wave input, the peak axial force of the upper chord is approximately 21% lower than that under the loading imposed by the 3D simulated waveforms. Additionally, the distribution of the axial forces of the lower chord member of the arch ring under the loading imposed by the 3D simulated waveforms and Rayleigh wave is similar, which differs from the trends observed during P–SV wave incidence. Specifically, when subjected to the loading imposed by the 3D simulated waveforms and Rayleigh wave, the axial forces of the lower chord members are relatively large at the crown and at a location approximately 1/10 of the arch span length from the arch foot along the arch ring. Under P–SV wave input, the maximum axial force of the lower chord member occurs at the arch foot.

From Figure 10b and Table 4, it can be observed that compared to the case with Rayleigh wave incidence, the bending moments of both the upper and lower chord members of the arch ring are slightly smaller when the fully 3D waveform solution is incident. The peak bending moment of the upper chord member of the arch ring is 0.80 times that of the Rayleigh wave incidence, and the peak bending moment of the lower chord member of the arch ring is 0.79 times that of the Rayleigh wave incidence. Compared to P–SV wave incidence, the peak bending moment of the lower chord member of the arch ring is amplified by 1.23 times when the fully 3D waveform solution is incident. The peak bending moments of the upper chord members for both cases are relatively close. For the lower chord member of the arch ring, the bending moment trends under the loading imposed by the 3D simulated waveforms and Rayleigh wave are similar, differing from those observed during P–SV wave incidence. Specifically, when subjected to the loading imposed by the 3D simulated waveforms and Rayleigh wave, the maximum bending moment occurs at the crown of the arch, followed by the location at 1/4 of the arch span length from the arch foot along the arch ring. When P–SV wave incidence, the bending moments are relatively large at both the arch feet and the crown.

From Figure 10c and Table 4, it can be observed that when the fully 3D waveform solution is incident, the shear forces of both the upper and lower chord members of the arch ring are smaller than in the other two cases. The peak shear forces of the upper and lower chord members of the arch ring are 0.53 times and 0.52 times that of the Rayleigh wave incidence, respectively, and 0.52 times and 0.55 times that of the P–SV wave incidence. The shear force distribution of the lower

TABLE 4 | Peak value internal forces of arch ring.

Peak internal forces, kN/kN·m		Fully 3D waveform solution	Rayleigh wave	P–SV wave	γ_{SR}	γ_{SS}
Upper chord member	Axial force	13,930.80	19,663.40	11,066.90	0.71	1.26
	Bending moment	1190.80	1490.64	1174.59	0.80	1.01
	Shear force	413.18	777.40	795.01	0.53	0.52
Lower chord member	Axial force	14,198.10	18,986.60	13,937.60	0.75	1.02
	Bending moment	942.32	1190.70	763.82	0.79	1.23
	Shear force	261.75	499.71	478.88	0.52	0.55

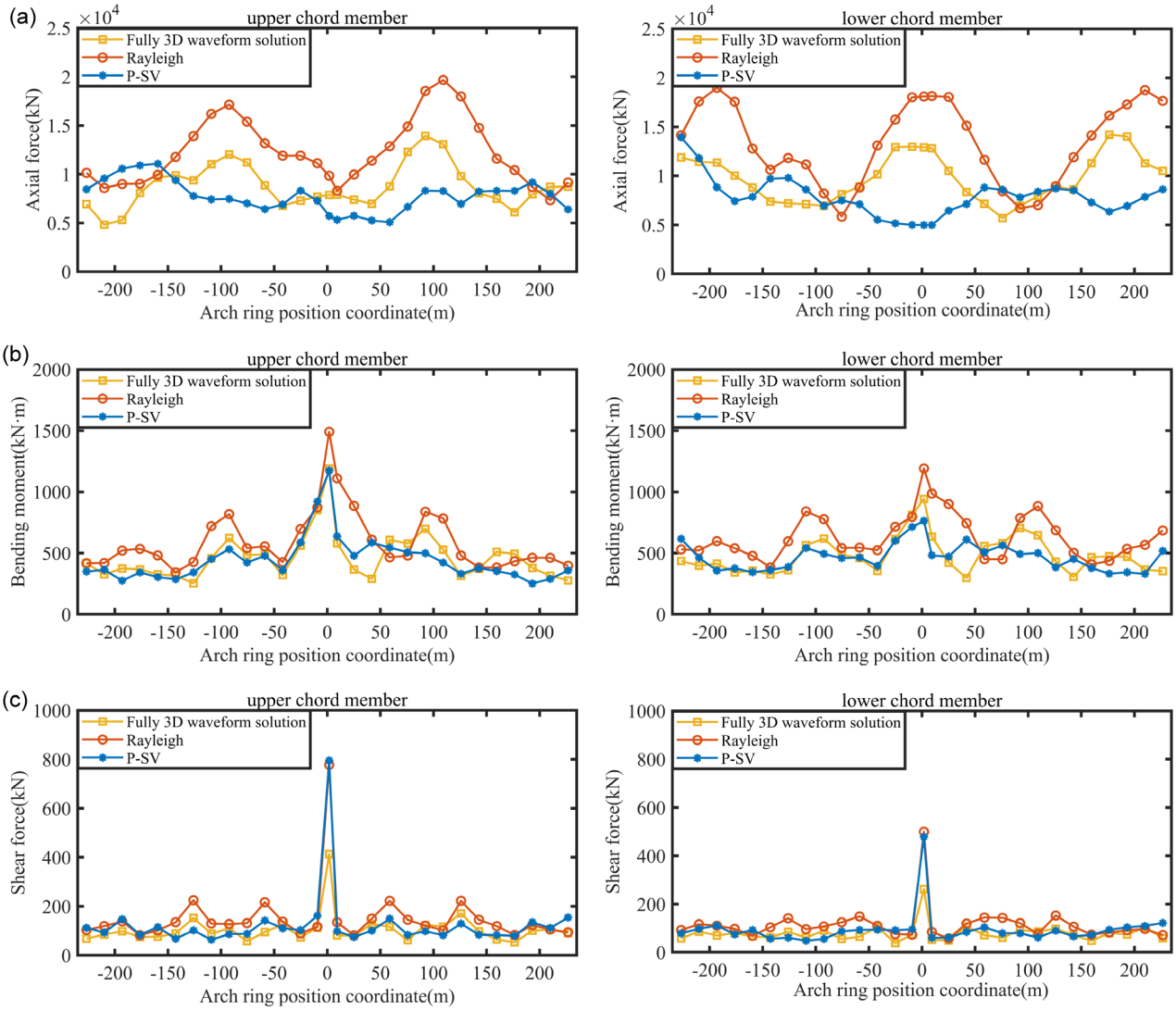

FIGURE 10 | Comparison of the axial forces, bending moments, and shear forces of the upper/lower chord member of the arch ring under the scenario with a 10 km epicentral distance: (a) axial force, (b) bending moment, and (c) shear force.

chord member of the arch ring under the loading imposed by the 3D simulated waveforms, Rayleigh wave, and P–SV wave is similar, with the peak shear force occurring at the crown of the arch in all cases.

To enhance the generalizability of the study, in addition to the initially selected scenario with an epicentral distance of 10 km, this article also considers a range of other epicentral distances. Accordingly, additional scenarios with epicentral distances of 6, 8, 12, 14, 16, 18, and 20 km are included to evaluate the sensitivity of the bridge response to varying epicentral distances. To maintain physical consistency across scenarios, epicentral distances of 0–4 km were excluded. Because in this range, the bridge would either cross the fault rupture zone or lie within the surface projection of the fault plane (Rjb = 0), which differs fundamentally from typical near-fault ground motions. Figure 11 presents the trends in internal forces of the lower chord members of the main arch ring under the 3D simulated waveforms, Rayleigh wave, and P–SV wave at different epicentral distances. From Figure 11, it can be seen that for different epicentral distance scenarios, the variation trend of internal forces in the lower chord members of the arch ring is consistent with that observed in the 10 km epicentral distance case.

Overall, the internal forces of the bridge differ depending on the type of input motion: Rayleigh waves generally induce the largest axial forces in most epicentral distance scenarios, and the fully 3D waveform solution produces more pronounced axial forces in several cases (such as at epicentral distances of 14 and 20 km). These results indicate that the waveform type and the propagation path jointly influence the structural response. Therefore, simplified waveform models may either underestimate or overestimate the actual structural demands under specific seismic scenarios.

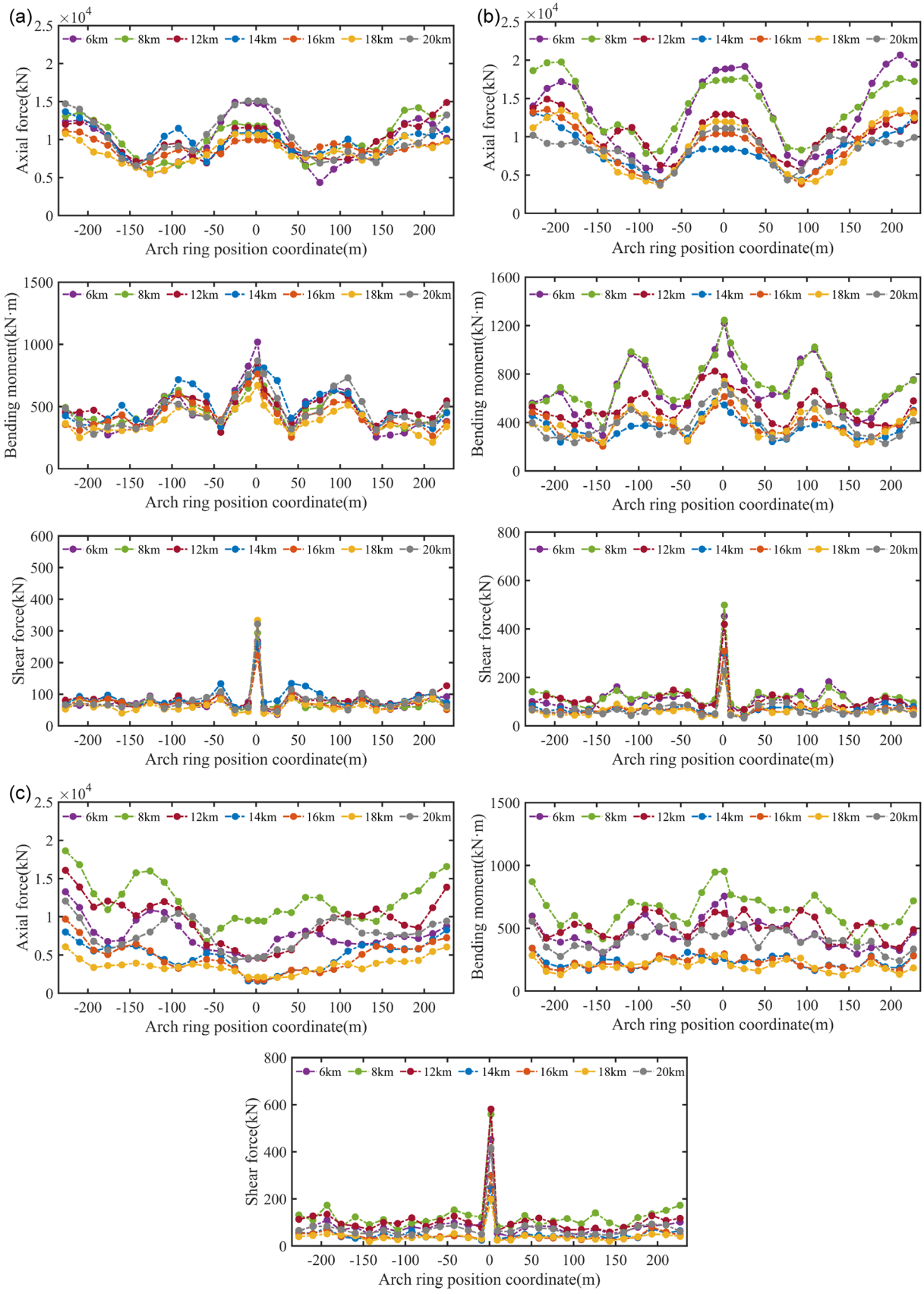

FIGURE 11 | Comparison of internal forces in the lower chord members of the arch ring under different epicentral distances: (a) internal force distribution under the fully 3D waveform solution, (b) internal force distribution under the Rayleigh wave, and (c) internal force distribution under the P–SV wave.

5.3.2 | Impact of Fully 3D Waveform Solution on Bridge Key Parts

To further analyze the seismic response of the bridge structure under the influence of the fully 3D waveform solution, the study focuses on key locations of the bridge structure discussed in section impact of fully 3D waveform solution on arch ring internal forces. Specifically, the analysis will examine the time histories of the axial force and bending moment at the arch foot of the lower chord member of the arch ring, where the largest amplitudes occur for all three types of wave incidence.

Figure 12 shows the axial force and bending moment time history at the arch foot position of the lower chord member of the arch ring under the scenario with a 10 km epicentral distance. From Figure 12, it can be observed that the axial force and bending moment at the arch foot are greatest for the Rayleigh wave, followed by the fully 3D waveform solution, with the P–SV wave causing the smallest response. The timing of the peaks in the axial force and bending moment at the arch foot differs from the three types of waves. For the P–SV wave, the peak occurs at the first wave crest, around 4.4 s. In contrast, for the fully 3D waveform solution and Rayleigh wave, the peaks in the axial force and bending moment occur after the first wave crest, at approximately 7.7 and 8.5 s, respectively. Additionally, a prolonged oscillation is observed for fully 3D waveform solution and Rayleigh wave incidences, indicating that these waves have excited a certain natural frequency of the bridge. The oscillation exhibits a larger amplitude under Rayleigh wave incidence compared to the fully 3D waveform solution and P–SV wave. The time history curves show that for the fully 3D waveform solution, five peaks occur between 8.8 and 12.5 s, while for the Rayleigh wave, five peaks are observed between 8.4 and 12.1 s. This allows the calculation of the excited bridge mode frequency, which is approximately 1.35 Hz.

Table 5 lists the first 20 modal frequencies and normalized mode participation factors of the bridge structure to determine the mode frequencies excited by the fully 3D waveform solution and Rayleigh wave. Both the fully 3D waveform solution and Rayleigh wave excite the 13th mode of the bridge, which has a natural frequency of 1.36 Hz.

To further analyze the axial force and bending moment time histories at the arch foot, the frequency response functions of the axial force at the lower chord member of the arch ring under the scenario with a 10 km epicentral distance are plotted relative to the input ground motion for the fully 3D waveform solution, Rayleigh wave, and P–SV wave, as shown in Figure 13. From the figure, it can be observed that in the frequency range above the fundamental frequency (0.22 Hz), the incidence of fully 3D waveform solution displays three significant peaks at 0.40, 1.33, and 1.67 Hz, corresponding to the 2nd, 13th, and 18th natural frequencies of the structure. For Rayleigh wave incidence, three significant peaks occur at 0.40, 1.33, and 1.73 Hz, corresponding to the 2nd, 13th, and 20th natural frequencies. For P–SV wave incidence, four significant peaks are present at 0.40, 1.00, 1.33, and 1.67 Hz, corresponding to the 2nd, 11th, 13th, and 18th natural frequencies. The amplitude of the frequency response functions varies significantly for the three input methods under the scenario with a 10 km epicentral distance: (1) For fully 3D waveform solution incidence, large amplitudes occur near the first mode in the longitudinal direction (0.44 Hz) and the first rotational mode in the transverse direction (1.36 Hz). (2) For Rayleigh wave incidence, the first three rotational mode frequencies of the bridge are significantly amplified. The largest amplitude occurs near the first mode in the transverse direction (1.36 Hz), with the second largest near the second mode (0.44 Hz). Additionally, under Rayleigh wave incidence, the amplitude of the higher-order mode (13th mode at 1.33 Hz) can exceed that of the lower-order mode (2nd mode at 0.44 Hz). (3) For P–SV wave incidence, to maintain consistency with the fully 3D waveform solution and Rayleigh wave, the seismic motion is applied along the longitudinal and vertical directions of the bridge. Significant amplitudes occur near the first two modes in the longitudinal direction (0.44 and 1.13 Hz) and the first two modes in the vertical direction (1.36 and 1.66 Hz). The largest amplitude occurs near the first longitudinal mode (0.44 Hz).

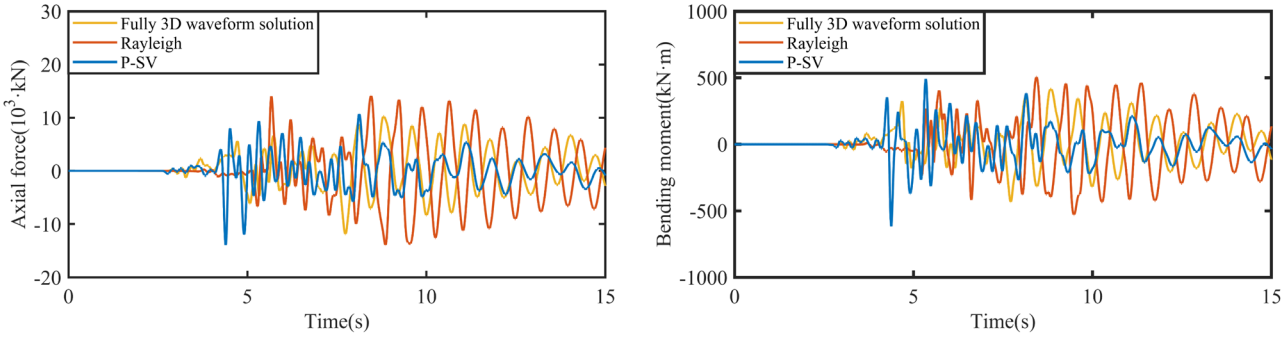

FIGURE 12 | Comparison of time response of axial force and bending moment of arch under the excitation of fully 3D waveform solution, Rayleigh wave, and P–SV wave.

TABLE 5 | Modal frequencies and normalized vibration participation coefficients of the bridge structure.

Mode	Frequency, Hz	*X* (transverse direction)	*Y* (longitudinal direction)	*Z* (vertical direction)	ROTX (transverse rotational direction)	ROTY (longitudinal rotational direction)	ROTZ (around the vertical direction)
1	0.22	1.00	0.00	0.00	0.00	0.65	1.00
2	0.44	0.00	1.00	0.00	0.52	0.00	0.00
3	0.45	0.00	0.00	0.00	0.00	0.00	0.43
4	0.66	0.49	0.00	0.00	0.00	0.57	0.48
5	0.68	0.00	0.00	0.13	0.13	0.00	0.00
6	0.83	0.02	0.00	0.00	0.00	0.03	0.01
7	0.95	0.33	0.00	0.00	0.00	1.00	0.33
8	1.01	0.00	0.29	0.01	0.01	0.00	0.00
9	1.03	0.00	0.20	0.01	0.03	0.00	0.00
10	1.05	0.00	0.00	0.00	0.00	0.00	0.34
11	1.13	0.00	0.63	0.00	0.34	0.00	0.00
12	1.20	0.22	0.00	0.00	0.00	0.45	0.22
13	1.36	0.00	0.00	1.00	1.00	0.00	0.00
14	1.37	0.21	0.00	0.00	0.00	0.48	0.21
15	1.38	0.01	0.00	0.00	0.00	0.03	0.01
16	1.57	0.00	0.00	0.00	0.00	0.00	0.14
17	1.61	0.09	0.00	0.00	0.00	0.32	0.09
18	1.66	0.00	0.17	0.84	0.83	0.00	0.00
19	1.70	0.00	0.38	0.45	0.44	0.00	0.00
20	1.75	0.00	0.15	0.20	0.22	0.00	0.00

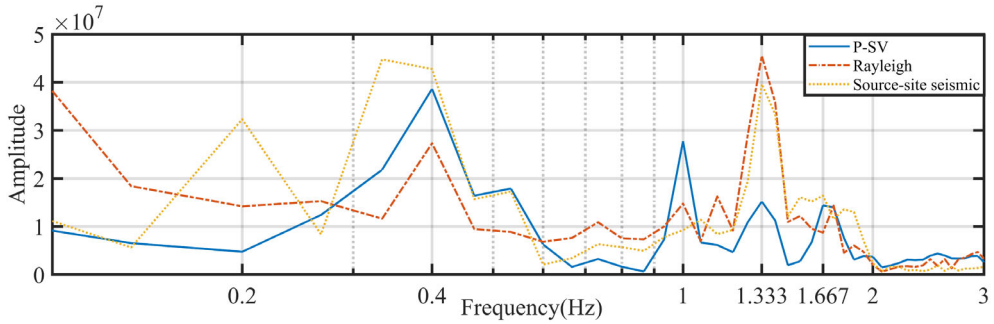

FIGURE 13 | Transfer function of the axial force of the arch foot under the scenario with a 10 km epicentral distance.

Figure 14 compares the axial force frequency response functions at the arch foot of the lower chord under three types of seismic waves across various epicentral distances. As shown in the figure, the frequency response patterns at most epicentral distances are consistent with those observed at 10 km. Specifically, under the action of the fully 3D waveform solution, significant response peaks appear near 0.4 and 1.36 Hz across most epicentral distances. For Rayleigh wave excitation, the frequency response also shows prominent peaks near 1.36 Hz in most cases. Notably, the Rayleigh wave induces a response where higher-order vibration modes in the excitation direction (11th mode at 1.13 Hz and 13th mode at 1.33 Hz) exhibit greater amplitudes than the lower-order mode (2nd mode at 0.44 Hz). Under P–SV wave excitation, the frequency response function generally exhibits its maximum amplitude near the first longitudinal mode of the bridge (0.44 Hz), with additional distinct peaks observed near 0.44, 1.13, 1.36, and 1.66 Hz. However, at several epicentral

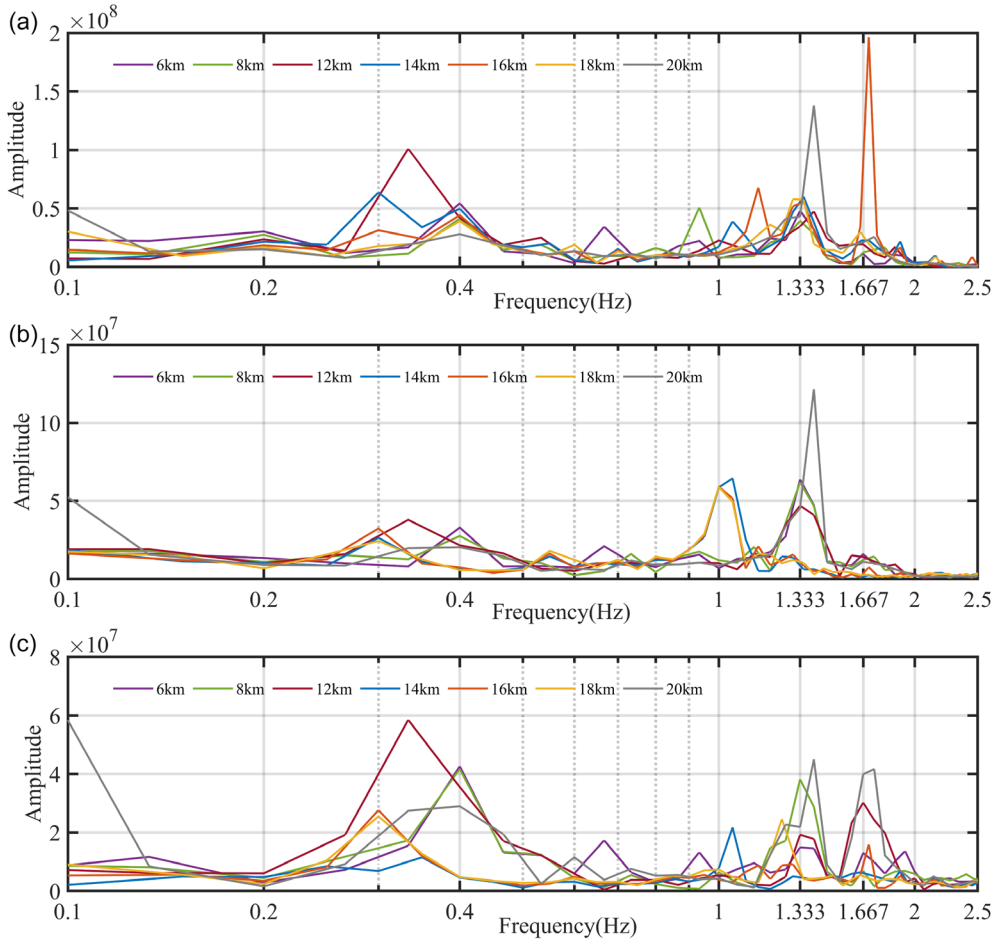

FIGURE 14 | Transfer function of the axial force of the arch foot under different epicentral distances: (a) transfer function under the fully 3D waveform solution, (b) transfer function under the Rayleigh wave, and (c) transfer function under the P–SV wave.

distances (e.g., 14 and 20 km), the amplitude near the first longitudinal mode of the bridge (0.44 Hz) is smaller than that near the fourth longitudinal mode (1.01 Hz) and the first vertical mode (1.36 Hz), respectively. To investigate the underlying causes, the Fourier spectra of the input ground motions under P–SV wave excitation were plotted, as shown in Figure 15. It can be observed that at 1.04 Hz, the Fourier amplitude for the 14 km epicentral distance is the lowest. This results in localized vibration at the arch foot, causing the frequency response amplitude at 1.04 Hz to exceed that near the first longitudinal mode (0.44 Hz). Similarly, at 1.399 Hz, the Fourier amplitude for the 20 km epicentral distance is the lowest, which excites the vertical bending mode, leading to a greater frequency response amplitude at 1.399 Hz than that near the first longitudinal mode (0.44 Hz).

In summary, the fully 3D waveform solution primarily excites the longitudinal and transverse rotational modes of the bridge. Rayleigh wave incidence mainly excites the transverse rotational modes, while P–SV wave incidence primarily

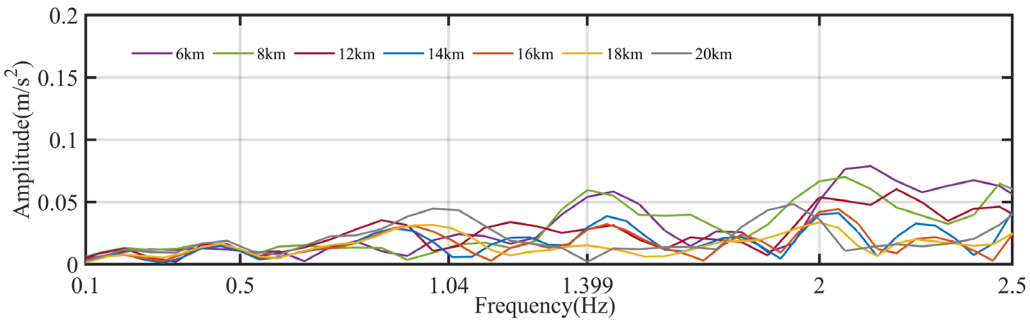

FIGURE 15 | Fourier amplitude spectra of input P–SV waves under different epicentral distances.

activates the longitudinal modes. At the higher-order mode (13th mode at 1.33 Hz), the axial force frequency response amplitudes show significant differences among the three wave types. For epicentral distances in the range of 6 to 12 km, the Rayleigh wave produces the largest amplitude, followed by the fully 3D waveform solution, with the P–SV wave generating the smallest amplitude. In contrast, for epicentral distances between 14 and 20 km, the amplitude under the fully 3D waveform solution surpasses that of the Rayleigh wave. The dynamic response of the bridge structure is governed by higher-order vibration modes, which leads to the possibility that simplified seismic waves may underestimate or overestimate the actual structural demands under specific scenarios.

6 | Conclusion

This study focuses on a steel–concrete arch bridge spanning a valley. By analyzing the seismic responses of the bridge under the fully 3D waveform solution, Rayleigh wave, and P–SV wave, the internal force distribution in the main arch ring and at the arch foot is examined. The main conclusions are summarized as follows:

1) The three types of wave incidences primarily excite different modal orders in the bridge structure. The fully 3D waveform solution primarily excites longitudinal and transverse rotational modes. The Rayleigh wave mainly excites transverse rotational modes. The P–SV wave primarily excites longitudinal and vertical modes.
2) Due to the different primary modes excited by the three wave types, there are significant differences in the distribution of the peak internal forces in the main arch ring of the bridge. When subjected to the loading imposed by the 3D simulated waveforms, peak axial forces are mainly concentrated at the crown and near the arch feet. Under Rayleigh wave incidence, the distribution of peak axial forces is the same as that under the loading imposed by the 3D simulated waveforms. Under P–SV wave incidence, peak axial forces are primarily concentrated at the arch feet.
3) The structural response is jointly influenced by the type of seismic waves and their propagation paths. Under certain scenarios, simplified ground motion inputs may lead to underestimation or overestimation of the actual structural response. In seismic response analysis of valley-spanning bridges, relying solely on Rayleigh or P–SV waves as input could fail to accurately capture the true force characteristics. Therefore, in practical seismic design, it is recommended, if possible, to adopt physics-based ground motion simulation methods that consider the rupture characteristics of the seismic source and its spatial relationship with the bridge structure.

In summary, both fully 3D waveform solution incidence and Rayleigh wave incidence induce nonuniform characteristics in the ground motion at the bridge site. The fully 3D waveform solution input can excite both low-order longitudinal modes and high-order rotational modes of the bridge, leading to an amplification of the structural dynamic response, which significantly impacts the seismic response of valley-spanning bridges. As a foundational step, this study focuses on a representative scenario that is physically realistic. Future work will introduce a broader range of rupture parameters for further investigation.

Author Contributions

Chao Luo: conceptualization, methodology, writing – original draft, funding acquisition. **Jingjing Li**: writing – original draft, investigation, software, visualization. **Zhipeng Zhao**: supervision, writing – review and editing. **Hao Wang**: supervision, funding acquisition, writing – review and editing.

Funding

The authors disclosed receipt of the following financial support for the research, authorship, and/or publication of this article: This research was supported by the Natural Science Foundation of Hebei Province (CN) (grant nos. E2022210095 and E2024210049), the S&T Program of Hebei (CN) (grant nos. 21375407D and 216Z5402G), the National Natural Science Foundation of China (grant no. 52378171), the Earthquake Science and Technology Program of Hebei Province (grant no. DZ2023120500009 and DZ2025092800001), and the Scientific Research Project of Higher Education Institutions in Hebei Province (grant no. CXZX2025050).

Conflicts of Interest

The authors declare no conflicts of interest.

Data Availability Statement

All data generated or analyzed during this study are available at https://doi.org/10.5281/zenodo.14723892.

References

Ba, Z., and J. Liang. 2015. "3-d Seismic Responses for Oblique Incident Rayleigh Waves of a Canyon Cut in a Layered Half-Space." *Journal of Vibration Engineering* 28, no. 5: 809–821.

Betti, R., A. Abdel-Ghaffar, and A. Niazy. 1993. "Kinematic Soil–structure Interaction for Long-Span Cable-Supported Bridges." *Earthquake Engineering & Structural Dynamics* 22, no. 5: 415–430.

Chiou, B. J., and R. Youngs. 2008. "An Nga Model for the Average Horizontal Component of Peak Ground Motion and Response Spectra." *Earthquake Spectra* 24, no. 1: 173–215.

Chouw, N., and H. Hao. 2008. "Significance of Ssi and Nonuniform Near-Fault Ground Motions in Bridge Response i: Effect on Response with Conventional Expansion Joint." *Engineering Structures* 30, no. 1: 141–153.

Ding, H., C. Zhu, and Y. Yu. 2017. "Characteristic of Ground Motions of a Canyon Topography under Inclined p and Sv Waves." *Chinese Journal of Vibration and Shock* 36: 88–92.

Efthymiou, E., and A. Camara. 2022. "Multi-Angle and Nonuniform Ground Motions on Cable-Stayed Bridges." *Earthquake Spectra* 38, no. 2: 1438–1462.

Gao, Y., D. Dai, and N. Zhang. 2021. "Progress and Prospect of Topographic Amplification Effects of Seismicwave in Canyon Sites." *Journal of Disaster Prevention and Mitigation Engineering* 41: 734–752.

Gatti, F., S. Touhami, F. Lopez-Caballero, et al. 2018. "Broad-Band 3-d Earthquake Simulation at Nuclear Site by an All-Embracing Source-to-Structure Approach." *Soil Dynamics and Earthquake Engineering* 115: 263–280.

Girmay, N., A. Poulos, and E. Miranda. 2024. "Evaluation of Directionality in Physics-Based Ground Motion Simulations of Strike-Slip Earthquakes." *Earthquake Spectra* 0, no. 0: 87552930241270555.

Graves, R. W., and A. Pitarka. 2010. "Broadband Ground-Motion Simulation Using a Hybrid Approach." *Bulletin of the Seismological Society of America* 100, no. 5A: 2095–2123.

Graves, R., and A. Pitarka. 2004. "Broadband Time History Simulation Using a Hybrid Approach." In *Proceedings of the 13th World Conference on Earthquake Engineering*.

Graves, R., and A. Pitarka. 2015. "Refinements to the Graves and Pitarka, 2010 Broadband Ground-Motion Simulation Method." *Seismological Research Letters* 86, no. 1: 75–80.

Graves, R., and A. Pitarka. 2016. "Kinematic Ground-Motion Simulations on rough Faults including Effects of 3d Stochastic Velocity Perturbations." *Bulletin of the Seismological Society of America* 106, no. 5: 2136–2153.

Gu, Y., and Z. Yu. 2011. "A Pile-Soil-Bridge Structure with Dynamic Interaction under Rayleigh Wave Excitation." *Chinese Journal of Vibration and Shock* 30, no. 12: 98–102.

He, J., Y. Wang, Y. Luo, S. Cao, and Z. He. 2015. "Monitoring Result Analysis of Slope Seismic Response during the Kangding ms6. 3 Earthquake." *China Journal of Engineering Geology* 23, no. 3: 383–393.

Jia, H., W. Wu, L. Xu, Y. Zhou, S. Zheng, and C. Zhao. 2024. "Numerical Simulation and Damaged Analysis of a Simply-Supported Beam Bridge Crossing Potential Active Fault." *Engineering Structures* 301: 117283.

Kenawy, M., D. McCallen, and A. Pitarka. 2023. "Characteristics and Selection of Near-Fault Simulated Earthquake Ground Motions for Nonlinear Analysis of Buildings." *Earthquake Spectra* 39, no. 4: 2281–2322.

Kuhlemeyer, R. L., and J. Lysmer. 1973. "Finite Element Method Accuracy for Wave Propagation Problems." *Journal of the Soil Mechanics and Foundations Division* 99, no. 5: 421–427.

Latečki, H., I. Molinari, and J. Stipčević. 2021. "3d Physics-Based Seismic Shaking Scenarios for City of Zagreb, Capital of croatia." *Bulletin of Earthquake Engineering* 20: 167–192.

Li, M., Z. Yang, M. Sun, and Y. Yang. 2023. "Influence of Canyon Topography Amplification Effect and Shielding Effect on Bridge Seismic Response." *Archive of Applied Mechanics* 93, no. 9: 3327–3340.

Li, Z., W. Wu, J. Li, and J. Zhao. 2022. "Dynamic Tensile Failure of a v-Shaped Canyon Induced by Vertically Travelling sv Waves." *Soil Dynamics and Earthquake Engineering* 162: 107458.

Liu, G., D. Jiang, Z. Liu, and X. Li. 2021. "Theory of Sv-Wave Multi-Support Seismic Excitations by a Layered Circular-Arc Canyon and Study on the Damage Mode of Bridge." *China Journal of Highway and Transport* 34, no. 11: 129–141.

Liu, J., and B. Li. 2006. "Dynamic Response Analysis of Underground Structures during Propagation of Rayleigh Waves." *Chinese Journal of Engineering Mechanics* 23, no. 10: 132–135 131.

Luo, C., C. Sheng, J. Wan, C. Xu, H. Guo, and H. Wang. 2024. "Study on the Effect of Rayleigh Waves on the Seismic Response of a v-Valley Arch Bridge." *China Journal of Highway and Transport* 37, no. 08: 135–146.

Luo, C., J. Li, H. Wang, X. Rong, and X. Wang. 2026. "A Magnitude-Based Incremental Dynamic Analysis Method for Seismic Performance Assessment of Near-Fault Structures." *Civil Engineering Sciences* 2. https://doi.org/10.34133/cesci.0011.

Luo, C., M. Lou, G. Gui, and H. Wang. 2019. "A Modified Domain Reduction Method for Numerical Simulation of Wave Propagation in Localized Regions." *Earthquake Engineering and Engineering Vibration* 18: 35–52.

Luo, C., X. Cao, Y. Gao, F. Xu, H. Feng, and H. Wang. 2024. "Applicability Study of the GP Fault Rupture Model in Strong Ground Motion Simulation for the Qinghai Menyuan MS 6.9 Earthquake." *Chinese Journal of Geophysics* 67, no. 2: 534–547.

Luzón, F., F. Sánchez-Sesma, J. Rodríguez-Zäñiga, et al. 1997. "Diffraction of p, s and Rayleigh Waves by Three-Dimensional Topographies." *Geophysical Journal International* 129: 571–578.

McCallen, D., A. Petersson, A. Rodgers, et al. 2021. "Eqsim—a Multidisciplinary Framework for Fault-to-Structure Earthquake Simulations on Exascale Computers Part i: Computational Models and Workflow." *Earthquake Spectra* 37, no. 2: 707–735.

McCallen, D., F. Petrone, M. Miah, A. Pitarka, A. Rodgers, and N. Abrahamson. 2021. "Eqsim—a Multidisciplinary Framework for Fault-to-Structure Earthquake Simulations on Exascale Computers, Part ii: Regional Simulations of Building Response." *Earthquake Spectra* 37, no. 2: 736–761.

Petersson, N. A., and B. Sjögreen. 2017a. Sw4, version 2.0. Computational Infrastructure of Geodynamics.

Petersson, N. A., and B. Sjögreen. 2017b. User's Guide to sw4, version 2.0. Lawrence Livermore National Laboratory.

Pitarka, A., R. Graves, K. Irikura, et al. 2022. "Refinements to the Graves–pitarka Kinematic Rupture Generator, including a Dynamically Consistent Slip-Rate Function, Applied to the 2019 mw 7.1 ridgecrest Earthquake." *Bulletin of the Seismological Society of America* 112, no. 1: 287–306.

Pitarka, A., R. Graves, K. Irikura, K. Miyakoshi, and A. Rodgers. 2020. "Kinematic Rupture Modeling of Ground Motion from the m7 Kumamoto, japan Earthquake." *Pure and Applied Geophysics* 177: 2199–2221.

Podestá, L., E. Sáez, G. Yáñez, and F. Leyton. 2019. "Geophysical Study and 3-d Modeling of Site Effects in Viña Del Mar, chile." *Earthquake Spectra* 35, no. 3: 1329–1349.

Rodgers, A., A. Pitarka, R. Pankajakshan, B. Sjögreen, and N. Petersson. 2020. "Regional-Scale 3d Ground-Motion Simulations of mw 7 Earthquakes on the Hayward Fault, Northern California Resolving Frequencies 0-10 Hz and including Site-Response Corrections." *Bulletin of the Seismological Society of America* 110, no. 6: 2862–2881.

Rosti, A., C. Smerzini, R. Paolucci, A. Penna, and M. Rota. 2023. "Validation of Physics-Based Ground Shaking Scenarios for Empirical Fragility Studies: The Case of the 2009 l'aquila Earthquake." *Bulletin of Earthquake Engineering* 21, no. 1: 95–123.

Sextos, A., A. Kappos, and K. Pitilakis. 2003. "Inelastic Dynamic Analysis of Rc Bridges Accounting for Spatial Variability of Ground Motion, Site Effects and Soil–structure Interaction Phenomena. Part 2: Parametric Study." *Earthquake Engineering & Structural Dynamics* 32, no. 4: 629–652.

Sjögreen, B., and N. A. Petersson. 2012. "A Fourth Order Accurate Finite Difference Scheme for the Elastic Wave Equation in Second Order Formulation." *Journal of Scientific Computing* 52: 17–48.

Somaini, D. R. 1987. "Seismic Behaviour of Girder Bridges for Horizontally Propagating Waves." *Earthquake Engineering & Structural Dynamics* 15, no. 6: 777–793.

Verret, D., D. LeBœuf, and É. Péloquin. 2021. "Site Effects of the Denis-Perron Dam (sm-3): A Case Study in Eastern North america." *Earthquake Spectra* 37, no. 1_suppl: 1602–1625.

Wang, F., Y. Zhang, X. Lin, and Z. Ba. 2024. "City-Scale Buildings Damage Estimation Based on Broadband Physics-Based Ground Motion Simulation of 2021 ms 6.4 yangbi, China, Earthquake." *Earthquake Spectra* 40, no. 1: 446–468.

Wang, Y., and Q. Chen. 2016. "Seismic Waves Inversion and Dynamic Response Analysis of Underground Structures." *Chinese Journal of Engineering Mechanics* 33, no. S1: 227–233.

Wang, Y., Y. Liu, and Y. Luo. 2018. Study on Seismic Response of Slope in Deep-Cut Canyon. Science Press.

Wong, H. 1982. "Effect of Surface Topography on the Diffraction of p, Sv, and Rayleigh Waves." *Bulletin of the Seismological Society of America* 72: 1167–1183.

Xiong, M., Y. Huang, and Q. Zhao. 2018. "Effect of Travelling Waves on Stochastic Seismic Response and Dynamic Reliability of a Long-Span Bridge on Soft Soil." *Bulletin of Earthquake Engineering* 16: 3721–3738.

Yue, Q., and J. Li. 2008. "Response Analysis of Underground Integrated Corridors under the Action of Approximate Rayleigh Seismic Waves." *Chinese Journal of Disaster Prevention and Mitigation Engineering* 28, no. 04: 409–416.

Zhang, F., S. Li, J. Wang, and J. Zhang. 2020. "Effects of Fault Rupture on Seismic Responses of Fault-Crossing Simply-Supported Highway Bridges." *Engineering Structures* 206: 110104.

Zhang, N., L. Wang, Y. Zhang, et al. 2024. "Effect of a v-Shaped Canyon on the Seismic Response of a Bridge under Oblique Incident Sh Waves." *Earthquake Engineering & Structural Dynamics* 53, no. 1: 496–514.

Zhang, W., P. Chen, J. Crempien, A. Kurtulus, P. Arduino, and E. Taciroglu. 2023. "Regional-Scale Seismic Fragility, Loss, and Resilience Assessment Using Physics-Based Simulated Ground Motions: An Application to Istanbul." *Earthquake Engineering & Structural Dynamics* 52, no. 6: 1785–1804.

Zhao, W., W. Chen, D. Yang, H. Gao, and P. Xie. 2022. "Analytical Solution for Seismic Response of Tunnels with Composite Linings in Elastic Ground Subjected to Rayleigh Waves." *Soil Dynamics and Earthquake Engineering* 153: 107113.

Zhou, G., X. Li, and X. Qi. 2010. "Seismic Response Analysis of Continuous Rigid Frame Bridge considering Canyon Topography Effects under Incident Sv Waves." *Earthquake Science* 23: 53–61.